This is the accepted manuscript made available via CHORUS. The article has been published as:

Energy Loss in Organic Photovoltaics: Nonfullerene Versus Fullerene Acceptors

Xiao Liu, Yongxi Li, Kan Ding, and Stephen Forrest

Phys. Rev. Applied **11**, 024060 — Published 25 February 2019

DOI: 10.1103/PhysRevApplied.11.024060

Energy Loss in Organic Photovoltaics: Non-fullerene vs. Fullerene Acceptors

Xiao Liu[1], Yongxi Li[1], Kan Ding[2], Stephen Forrest[1,2,3]

[1]Department of Electrical Engineering and Computer Science,

[2]Deparment of Physics, and [3]Department of Material Science and Engineering

University of Michigan, Ann Arbor, MI, 48109 United States

Abstract

The energy loss experienced by organic photovoltaics (OPVs) is the difference between the lowest photogenerated exciton energy of donor or acceptor and the open circuit energy. It sets a fundamental limit to the open circuit voltage and hence the efficiency of OPVs. This loss can be as large as 0.7 eV for fullerene acceptors, although non-fullerene acceptors (NFAs) reduce this to $\leq$ 0.6 eV. Here, we systematically quantify the relationship between charge transfer energy loss (ΔE_{CT}), non-radiative recombination loss, exciton binding energy, and intra- and inter-molecular electron-phonon couplings. Density functional theory and comprehensive quantum mechanical modeling is used to associate molecular volume, effective conjugation length, and the nonbonding character of molecules to these several energy losses. Nonradiative recombination in donor/NFA heterojunctions is quantified by the charge transfer state emission quantum yield, and its Frank-Condon shift. Our analytical results are consistent with measurements where ΔE_{CT} is varied between 0 and 0.6 eV using a variety of fullerene derivatives and thiophene-based NFAs paired with donor molecules. Molecular design rules to decrease the energy loss in OPVs derived from our analysis are provided.

I. Introduction

Excitons in organic semiconductors are tightly bound electron-hole pairs with binding energies of E_B = 0.2 to 1.5 eV. [1–4] A large driving force is required to overcome the binding energy to separate the electron and hole in the photocurrent generation process. This force is provided by the offset of the lowest unoccupied molecular orbital (LUMO) and highest occupied MO (HOMO) energies, i.e. ΔE_{LUMO} and ΔE_{HOMO}, respectively, between donor and acceptor molecules at a type-II heterojunction (HJ). As a result, the dissociation process incurs an energy loss during charge transfer (CT) at the interface:

$$\Delta E_{CT} = E_{ex} - E_{CT} \approx \Delta E_{HOMO(LUMO)} - E_B\,, \tag{1}$$

where E_{ex} is the lowest photogenerated exciton (S_1) energy of the donor or acceptor that is generally equal to the HOMO-LUMO energy gap less E_B. Also, E_{CT} is the CT state energy. Additional losses arise from both radiative (ΔE_r) and nonradiative (ΔE_{nr}) recombination at the heterojunction: [5]

$$\Delta E_{rec} = E_{CT} - qV_{OC} = \Delta E_r + \Delta E_{nr}, \tag{2}$$

where V_{OC} is the open circuit voltage and q is the electron charge. Therefore, the total energy loss at the donor-acceptor HJ is: [5]

$$E_{loss} = \Delta E_{CT} + \Delta E_{rec} = E_{ex} - qV_{OC}. \tag{3}$$

Heterojunctions employing fullerene derivatives usually suffer from a loss of E_{loss} > 0.7 eV. Alternatives to fullerene acceptors have therefore been sought to reduce E_{loss} while extending the absorption spectrum into the infrared. The development of nonfullerene acceptors (NFAs) with acceptor-donor-acceptor (a-d-a) or perylene diimide (PDI)-based molecular motifs give freedom to tune the molecular energetics, absorption spectra and thin film morphologies through

molecular design. [6–10] As a result, HJs using NFAs show ΔE_{CT} as low as 0.1 to 0.2 eV, ΔE_{nr} of 0.2 to 0.3 eV and a total E_{loss} approaching ≤0.6 eV, [11–15] compared to fullerene-based HJs with ΔE_{CT} > 0.3 eV, ΔE_{nr} of 0.3 to 0.4 eV. [16–18] While energy loss mechanisms have been discussed for years, [5,19–21] to our knowledge there has been no *quantitative* analysis as to why NFAs have both ΔE_{CT} and ΔE_{nr} comparatively low. As a result, unambiguous guidelines for molecular designs have been lacking.

In this work, we explore fundamental approaches to reduce both ΔE_{CT} and ΔE_{nr}, while also achieving a high exciton dissociation efficiency. We use semiclassical Marcus charge transfer theory to quantify both the charge transfer, k_{CT}, and non-radiative recombination, k_{nr}, rates. These rates are used to analyze the energy losses, ΔE_{CT} and ΔE_{nr}, as functions of E_B and the intra- and inter-molecular electron-phonon coupling. We compare the energy losses during exciton dissociation of a family of acceptors in type II bulk HJs (BHJs), where k_{CT} vs. ΔE_{CT} are studied using temperature dependent transient photoluminescence (PL) spectroscopy. Also, ΔE_{nr} is determined from the electroluminescence quantum yield of the CT states. The large and rigid molecular backbone of thiophene-based NFAs, and the presence of non-bonding orbitals introduced by cyano or chloro group substitutions extend the electron density distribution along the molecules to reduce E_B, electron-phonon coupling, and hence reduce energy losses. Calculations using density functional theory (DFT) and quantum mechanical modeling lead to strategies for the design of molecular structures with low energy losses.

II. Theory

We focus our attention on comparing charge transfer of excitons from a variety of acceptor to donor molecules. The transition from an acceptor exciton (A^*) to a CT state (A^-/D^+) is illustrated in Fig. 1(a). In semiclassical Marcus theory, [22,23] the rate for non-adiabatic transfer is given by:

$$k_{CT} = \frac{2\pi}{\hbar} V^2 F = \frac{2\pi}{\hbar} V^2 \left[\frac{1}{\sqrt{4\pi\lambda_O k_B T}} \sum_{n'} (-S) \frac{S^{n'}}{n'!} \exp\left(-\frac{\left(-\Delta E_{CT} + \lambda_O + n'\hbar\langle\omega_I\rangle\right)^2}{4\lambda_O k_B T}\right)\right]. \quad (4)$$

Here, $V = \langle\psi_{A^*D}|H|\psi_{A^-D^+}\rangle$ is the electronic coupling between the acceptor excited state (ψ_{A^*D}) and CT ($\psi_{A^-D^+}$) wavefunctions, H is the Hamiltonian, F denotes the nuclear Franck-Condon factor, λ_O is the intermolecular reorganization energy, k_B is the Boltzmann constant, and T is the temperature. Also, S is the mean intramolecular electron-phonon coupling constant known as the Huang-Rhys factor, given by $S = \lambda_I/\hbar\langle\omega_I\rangle$ where λ_I is the intramolecular reorganization energy incorporating all the coupled modes. Conveniently, the intramolecular phonon modes can be subsumed into a single mode with mean energy $\hbar\langle\omega_I\rangle$, since the dominant mode in organic molecules is carbon-carbon (C-C) bond stretching with $\hbar\langle\omega_I\rangle \approx 0.17$ eV. The Gibbs free energy in Eq. 4 is:

$$-\Delta E_{CT} = E_{CT} - E_{ex} \approx \left|E_{HOMO_{\mathrm{D}}} - E_{LUMO_{\mathrm{A}}}\right| - \left(\left|E_{HOMO_{\mathrm{A}}} - E_{LUMO_{\mathrm{A}}}\right| - E_B\right)$$

$$= -(\Delta E_{HOMO} - E_B), \quad (5)$$

where $E_{HOMO_{\mathrm{D(A)}}}$ and $E_{LUMO_{\mathrm{D(A)}}}$ are the HOMO and LUMO energies of the donor (acceptor) molecule, respectively. The contributions of other factors, such as entropy, are unlikely to vary significantly between our samples that have the same 2:98 acceptor:donor blend ratio (see Experimental section), and are therefore assumed to be constant offsets in Gibbs free energy that are excluded in the following analysis.

The Franck-Condon factor in Eq. 4 contains contributions from high frequency intramolecular phonon modes ($\hbar\omega_I \gg k_BT$) and low frequency intermolecular modes ($\hbar\omega_O \ll k_BT$) in the medium. The high frequency modes are treated assuming quantized levels (n = {0, 1, 2 …}) depicted in Fig. 1. This is due to temperature independent quantum mechanical tunneling through the barrier separating the initial and final states. Following Kasha's rule, it is assumed that the transition occurs from the lowest vibrational state ($n = 0$) of acceptor excitons (A^*) to the vibrational state n' in the CT (A^-/D^+) manifold, [24,25] since no change of k_{CT} is observed when using a shorter wavelength excitation source. The Frank-Condon integral of the tunneling transition is then simplified to $\exp(-S)\frac{S^{n'}}{n'!}$. Coupling of the initial and finial states via low frequency intermolecular modes is adequately described by the classical picture if the thermal energy is greater than the phonon energy, $\hbar\omega_O$, whose contributions are subsumed into λ_O in the Arrhenius-type exponential in Eq. 4.

The reorganization energy, λ, during charge transfer is the sum of intramolecular (λ_I) and intermolecular (λ_O) contributions. Intramolecular reorganization arises from local electron-phonon coupling leading to a nuclear coordinate displacement $\langle\Delta Q\rangle$ between two equilibrium positions Q_1 and Q_2 (or Q_2 and Q_3 in Fig. 1b). In the harmonic approximation,

$$\lambda_I = \frac{1}{2}(M\langle\omega_I\rangle^2)\langle\Delta Q\rangle^2, \tag{6}$$

$$S = \frac{1}{2}(\frac{M\langle\omega_I\rangle}{\hbar})\langle\Delta Q\rangle^2, \tag{7}$$

where M is the reduced nuclear mass of the molecule.

Intermolecular reorganization is due to the electronic polarization, and consequently lattice relaxation of the surrounding medium. Assuming a spherically symmetric charge

distribution on the donor and acceptor, and treating the medium as an isotropic dielectric continuum, we have: [26]

$$\lambda_O = \frac{e^2}{4\pi\varepsilon_0}\left(\frac{1}{\varepsilon_{opt}} - \frac{1}{\varepsilon_s}\right)\left(\frac{1}{2r_D} + \frac{1}{2r_A} - \frac{1}{R_{DA}}\right), \tag{8}$$

where ε_{opt} and ε_s are the optical and static dielectric constants, respectively, $r_{D(A)}$ is the effective radius of the donor (acceptor) molecule, and R_{DA} is the distance between acceptor and donor.

Non-radiative recombination energy losses (ΔE_{nr}) that occur through coupling from the CT (A^-/D^+) to the ground state (A/D) are illustrated in Fig. 1(b). The transfer rate is:

$$k_{nr} = \frac{2\pi}{\hbar} V'^2 \frac{1}{\sqrt{4\pi\lambda_O' k_B T}} \sum_{n''} (-S') \frac{S'^{n''}}{n''!} \exp\left(-\frac{\left(-E_{CT} + \lambda_O' + n''\hbar\langle\omega_I\rangle\right)^2}{4\lambda_O' k_B T}\right), \tag{9}$$

where, $V' = \langle\psi_{A^-D^+}|H|\psi_{AD}\rangle$ is the electronic coupling between the CT and ground states. The values of S' and λ_O' may differ from S and λ_O in Eq. 4 due to different magnitudes of electron-phonon coupling in the charge transfer and recombination processes that may involve different types of electronic states and numbers of molecules. The Gibbs free energy in Eq. 9 is equal to E_{CT}, leading to a nonradiative energy loss of: [27]

$$\Delta E_{nr} = k_B T \ln\left(\frac{1}{\eta_{EL}}\right) = k_B T \ln\left(\frac{k_r + k_{nr}}{k_r}\right), \tag{10}$$

Here, η_{EL} is the internal quantum efficiency of the CT state electroluminescence.

To achieve low energy loss yet efficient charge transfer, E_B and ΔE_{HOMO} must be minimized at the same time (c.f. Eqs. 4 and 5). Secondly, decreasing both intra- and intermolecular electron-phonon coupling leads to an increased k_{CT} at a minimum cost to ΔE_{CT},

as well as a decrease in k_{nr} and consequently, ΔE_{nr}. Calculations of k_{CT} and k_{nr} using Eqs. 4 and 9 at $T = 300\ K$ are shown in Fig. 2. For convenience, we set V^2 and V'^2 equal to unity. Figures 2(a) and (b) show that reducing λ_O and S, respectively, lead to an increased maximum in k_{CT} that occurs at a lower ΔE_{CT}. Note that k_{nr} vs. E_{CT} in Figs. 2(c) and (d) have a Marcus inverted relationship in the range of E_{CT} we consider. This is a version of the "energy gap law" [28] [20] where k_{nr} decreases with increasing E_{CT}. Decreasing λ_O and S further reduces k_{nr} at a given E_{CT}, and hence non-radiative recombination ΔE_{nr}, according to Eq. 10. All four figures show that a decrease of S results in a more pronounced change of k_{CT} and k_{nr} than that for λ_O.

III. Experimental

Molecular level electron density distributions of NFAs and fullerenes, and their energy levels were modeled using DFT/time-dependent DFT (TDDFT) in the Gaussian 09w package. [29] The calculation of exciton binding energy and reorganization energy was based on the B3LYP functional and the 6-31G(d) basis set, since B3LYP is one of the most widely used functional that has previously been shown to give results of molecular orbital levels, exciton and ionic states of NFAs that agree well with the measurements. [30–34] For example, the measured HOMO level and lowest-energy absorption peak of IT-IC are -5.51 eV and 1.75 eV, respectively, [6] as compared to -5.49 eV and 1.76 eV calculated using B3LYP. The exciton binding and reorganization energies of NFAs calculated using B3LYP are comparable with reported previously. [35,36] In this work, molecular solvation effects are considered by combining the DFT calculations with the Polarizable Continuum Model. [37]

The k_{CT} as a function of ΔE_{CT} was studied by blending the acceptors with a variety of donors at an acceptor concentration of 2 ± 1 wt%, and with a wide energy gap poly(methyl methacrylate) (PMMA) or Bathophenanthroline (Bphen) matrix as a reference. The mixture was either made by thermal evaporation at a chamber base pressure of $2x10^{-7}$ torr, or dissolved in chlorobenzene at a concentration of 20 mg mL^{-1}, and then spin-coated onto a Si substrate to form 100 nm thick films. Donors were chosen to have non-overlapping absorption spectra with the acceptors such that excitons are generated only on the acceptor molecules using appropriately chosen excitation wavelengths. In the dilute blends, the acceptor domains are small compared to the exciton diffusion length, thereby eliminating the dynamics of exciton diffusion. Then, k_{CT} is calculated from the difference between the acceptor exciton decay rates in the type-I PMMA(or Bphen)/acceptor HJ, and at the type-II donor/acceptor HJ.

Exciton dynamics were measured by time-resolved PL using a time-correlated single photon counter (PicoHarp 300, PicoQuant GmbH) coupled to a Si single photon avalanche detector (PDM Series, PicoQuant GmbH). The accepter molecules were excited at λ = 725 nm for NFAs, and 560 nm for fullerene derivatives using 150 fs pulses at a 1 kHz repetition rate from a Ti:sapphire laser (CPA-2110, Clark-MXR Inc.)-pumped optical parametric amplifier (TOPAS-C, Coherent). Charge transfer dynamics vs. temperature in the range between 295 K and 25 K were obtained in a closed-cycle cryostat (SHI-4-5, Janis Research Company LLC).

Organic photovoltaic cell structures were: indium tin oxide (ITO)/ZnO/BHJ/MoO_3/Al. The 20 nm thick ZnO layer was spin-coated onto a precleaned, UV-ozone-treated ITO anode, followed by 30 min thermal annealing at 150 ºC in air. The 100 nm thick BHJ layer was spin-coated on the ZnO, followed by thermal evaporation of a 10 nm thick MoO_3 buffer and a 100 nm thick Al cathode at a chamber base pressure of $2x10^{-7}$ torr. The external quantum efficiency was

measured using the photocurrent of devices coupled to a lock-in amplifier (Stanford Research Systems SR830) while being excited by monochromated light from a Xe arc-discharge lamp chopped at 200 Hz. Electroluminescence (EL) spectra of CT states were measured under forward bias using a fiber-coupled monochromator (Acton series SP2300i, Princeton Instruments) equipped with a Si charge-coupled device array (PIXIS:400, Princeton Instruments). Electroluminescence from individual donors and acceptors were measured using devices that replaced the blend layer with a neat acceptor or donor layer of the same thickness.

IV. Results

The parameters, E_B, S and λ_O in Eqs. 4, 5 and 9 that determine energy losses are closely correlated with the molecular structure. We, therefore, systematically analyzed the exciton binding energies, molecular polarizabilities and intramolecular reorganization of fullerenes and NFAs by DFT. The exciton binding energy is $E_B = (E_- + E_+) - (E_{gnd} + E_{ex})$, where E_- and E_+ are the optimized energies of radical anions and cations of the molecule, respectively. Also, E_{gnd} and E_{ex} are the ground and first singlet excited state energies, respectively.

Figure 3 shows the molecular structures of archetypical a-d-a type NFAs. The electron-donating conjugate backbone is capped with two electron-withdrawing side groups. The electron and hole distributions of the excited state along the long molecular axis of BT-ClC is shown in Fig. 3(b). The conjugated electron system is shown by the bold red line bridging the electron-donating thiophene backbone to the electron deficient cyano and Cl groups. This charge distribution results in symmetric intramolecular charge transfer (ICT) from the middle to the two ends of the optically excited molecule. Also, the relative segregation of electron and hole

densities results in a reduced E_B (see below). Two other molecules with different numbers of thiophene rings, and hence a shorter conjugation length with reduced ICT are shown for comparison in Fig. 3(c).

Figure 4(a) shows calculated E_B of a variety of acceptors vs. the *effective molecular volume*. All the chemical names and structures of the molecules are provided in the Supplementary Information. [38] The effective molecular volume $v = l \cdot w \cdot h$ is determined from the molecular length l, width w, and height h that are defined by a box whose boundaries are defined at an electron density of 0.02 au^{-3}. Here, 0.02 au^{-3} is commonly used to define the iso-surface of electron distributions and the size of a molecule. [29] Figure 4(a) shows that E_B decreases with increasing v. Also, the slope of E_B vs. v decreases until v > 1.5 nm^3. Figure 4(b) shows the calculated static polarizabilities, α_{xx}, along the molecular length, l of this same population of acceptors. Since the electron distribution is spread along the molecular backbone, α_{xx} increases with l. This corresponds to the x coordinate, with y and z along w and h, respectively. The full polarizability tensors of the molecules are provided in the Supplementary Information. [38]

The intramolecular reorganization energy of electron transfer is $\lambda_I^- = (E_0^* - E_0) + (E_-^* - E_-)$, where E_0 and E_- are the energies of the neutral and radical anion molecules in their optimized geometries, respectively, and E_0^* and E_-^* are energies of the neutral and radical anion molecules in their unrelaxed geometries, respectively. Table 1 lists the calculated λ_I^- of $PC_{71}BM$ and the three a-d-a NFAs in Fig. 3(a) and (c). Non-fullerene acceptors have smaller intramolecular reorganization energies on electron transfer than $PC_{71}BM$. Introducing electron-

donating oxy-, and electron-withdrawing cyano-, and chloro- moieties (Fig. 3(a)), or extending the conjugation length of the donor subgroup (Fig. 3(c)) further reduces λ_I^-.

The k_{CT} from BT-ClC (or BT-IC), IT-IC and fullerene derivatives are measured as functions of ΔE_{CT}, with results shown in Fig. 5. The NFA-based HJs show non-monotonic changes of k_{CT} as ΔE_{CT} increases, indicative of the Marcus normal (non-shaded) and inverted (shaded) regimes that are separated by the ΔE_{CT} corresponding to the maximum value of k_{CT}. The k_{CT} of fullerene derivatives in Fig. 5(c), however, do not reach a maximum, but rather increase monotonically until ΔE_{CT} = 0.6 eV which is at energies short of the inverted region.

We also measured k_{CT} as a function of temperature for two HJs, BT-IC/PBDBT and IT-IC/PBDBT, with results shown in Fig. 6 (a) and (b), respectively. Both systems show two distinct regimes with a transition at $T_X = \sim 150$ K. At $T > T_X$, k_{CT} decreases rapidly with temperature, characteristic of thermally activated behavior for charge transfer. At $T < T_X$, k_{CT} is relatively temperature independent due to the dominance of tunneling in the charge transfer process.

We compared ΔE_{nr} in HJs employing NFAs and fullerenes by measuring the quantum efficiency of the CT state electroluminescence (η_{EL}) obtained by driving $PC_{71}BM$/PBDBT and IT-IC/PBDBT HJ devices in forward bias. In Supplementary Fig. S1, [38] we find that η_{EL} of IT-IC/PBDBT is approximately one order of magnitude higher than that of $PC_{71}BM$/PBDBT.

Nonradiative coupling between the CT and ground states possesses the same Franck-Condon factor as in radiative coupling [20]. We therefore measured the Franck-Condon shift between absorption and emission spectra of CT state to probe the electron-phonon coupling strength during the nonradiative recombination. Electroluminescence spectra of

$PC_{71}BM$/PBDBT and IT-IC/PBDBT OPVs in Fig. 7 show CT emission peaks at 1.24 ± 0.01 eV and 1.37 ± 0.01 eV, respectively. The peaks of EL_{blend} at 1.65 ± 0.01 eV in Fig. 7(a) and 1.60 ± 0.01 eV in Fig. 7(b) are due to the residual emission from PBDBT and ITIC, respectively. We extract the CT state emission spectra by subtracting EL spectrum of PBDBT in Fig. 7(a) and ITIC in Fig. 7(b) from that of the blend. This difference is normalized to the CT absorption spectra that are extracted from Gaussian fits to the external quantum efficiency spectra at the low energy shoulders using the same full width half maximum (FWHM) as the corresponding emission spectrum. [39] The Franck-Condon shift of the $PC_{71}BM$/PBDBT HJ is E_{FC} = 0.49 ± 0.02 eV, while for IT-IC/PBDBT, E_{FC} = 0.22 ± 0.02 eV.

V. Discussion

For a given offset of the donor and acceptor HOMO energies, the Gibbs free energy of hole transfer from acceptor to donor, ΔE_{CT}, is maximized by minimizing the acceptor exciton binding energy, which in turn increases k_{CT} in the Marcus non-inverted regime. The combined influences of molecular size, conjugation length, and strength of the electron donating and withdrawing groups determines the magnitude of ICT in the acceptors, [40,41] and this ultimately determines E_B. The molecular size and the availability of sp^2 hybridized atoms in the molecules determine the extent of conjugation, and hence the mean separation of the electron and hole orbital distributions. The rigid coplanar structure of a-d-a NFAs ensures that the electron wavefunction is delocalized over the entire molecular backbone, unlike polymers that can twist at C-C single bonds that ultimately terminates the extent of the excited state [42]. This is apparent from DFT calculations of the electron and hole densities of BT-CIC in Fig. 3(b). The

oscillations in the densities are due to variations in electron and hole wavefunctions at each of the thiophene rings that terminate at the end caps. The low electron concentration at the molecular center of mass relative to the capping groups results from their electron donating and withdrawing character, respectively, and leads to a reduction in the electron-hole (i.e. exciton) binding energy.

To estimate the effects of molecular size on the exciton binding energy, we use a simplified electron wavefunction for a particle in a three dimensional box, i.e. $\Psi_{n_x,n_y,n_z} = \sqrt{\frac{8}{v}} \sin\left(\frac{n_x \pi x}{l}\right) \sin\left(\frac{n_y \pi y}{w}\right) \sin\left(\frac{n_z \pi z}{h}\right)$, where n_x, n_y, n_z are quantum numbers. This fits the results in Fig. 4(a), whereby the E_B vs. effective molecular volume monotonically decreases, independent of the details of the molecules studied (i.e. fullerenes or NFAs). For this analysis, we use an average molecular height of h = 0.3 nm and width of w = 0.8 nm, and vary the length l according to the dimensions of the molecule. Then the wavefunctions Ψ_{n_x,n_y,n_z} and exciton binding energies are solved using Schrödinger's equation to give the binding energy:

$$E_B = q^2 \int \frac{|\Psi_{0,0,0}(\boldsymbol{r}_h)|^2 \cdot |\Psi_{1,0,0}(\boldsymbol{r}_e)|^2}{f \cdot 4\pi\varepsilon_0 |\boldsymbol{r}_h - \boldsymbol{r}_e|} d\boldsymbol{r}_h{}^3 d\boldsymbol{r}_e{}^3, \quad (11)$$

where the hole and electron wavefunctions are $\Psi_{0,0,0}$ and $\Psi_{1,0,0}$, respectively, $\boldsymbol{r}_h$ and $\boldsymbol{r}_e$ are the coordinate vectors of the hole and electron, respectively, and q is the electron charge. Here, f is a parameter that accounts for the relative dielectric constant of the molecule and the relaxation energy of ionic species. The solid line in Fig. 4a corresponds to only a single value of f = 5.4 that approximately fits the entire population of acceptors. This is indeed remarkable, given that the molecular structures vary significantly from molecule to molecule, and from highly symmetric fullerenes to planar NFAs. The shaded region depicts the 95% confidence band

between f = 6.8 and 4. The deviations of the data from the solid line are associated with details of the molecular structures that impact the molecular polarizabilities and relative dielectric constants in the solid.

As shown in Fig. 4(b), the polarizability α_{xx} vs. molecular length l follows an empirical power-law dependence: [43,44]

$$\alpha_{xx} = \alpha_0 + \alpha_1 l^n. \tag{12}$$

Here, α_0 is the polarizability of terminal bonds such as C-H, and α_1 is related to the polarizability of conjugated or non-conjugated chains of length l. A fit to the data gives $\alpha_0 = 0.035 \pm 0.075$ nm^3, $\alpha_1 = 0.098 \pm 0.060$ nm$^{3\text{-}n}$, and $n = 1.51 \pm 0.44$. A superlinear increase of polarizability ($n > 1$) is due to the contributions of conjugation and ICT [40]. The relationship between the dielectric constant of the medium and the polarizabilities of each constituent, α_i, is given by the Clausius-Mosotti relationship:

$$\frac{\varepsilon-1}{\varepsilon+2} = \frac{4\pi}{3}\sum_i \mathrm{N}_i\alpha_i \ . \tag{13}$$

where the molecular packing density is N_i. The effect of the dielectric constant change on E_B can be estimated using Eqs. 12 and 13 to replace constant f of Eq. 11, and assuming an isotropically polarizable medium comprising randomly oriented molecules with N = 1.3 nm^{-3}. This yields the blue dashed line in Fig. 4(a). Two blue dotted lines indicate the confidence limits of the calculation from the fit to the data in Fig. 4(b). The fit closely follows the data for molecules 1 to 11 compared to the that using a constant *f*, despite a slight overestimation due to simplifications used to approximate molecular structure and the molecular relaxation of ionic

species that are considered DFT calculations. The less accurate fits to molecules 12, 13, 15 - 17 is attributed to molecular bends that disturb the electron conjugation, thereby increasing E_B.

Achieving a small ΔE_{CT} and ΔE_{nr} requires simultaneously reducing both the intra- and intermolecular electron-phonon coupling. Increased dielectric constant of NFAs as shown above reduce the intermolecular coupling, λ_O (c.f. Eq. 8). The intramolecular coupling constant, S, also changes with the size and rigidity of the molecules. Equations 6 and 7 show that λ_I and S are proportional to $\langle \Delta Q \rangle^2$. Studies of oligoacenes, polythiophenes, fused thiophenes, etc. [45]. have shown that $\langle \Delta Q \rangle^2 \propto \frac{1}{N_{C-C}} \propto \frac{1}{n}$, where, N_{C-C} is the number of carbon-carbon bonds, and n is the number of aromatic rings. Bond length adjustment is smaller when accommodating a more delocalized charge distribution. In NFAs, extending the conjugation length along the donor subgroup is one such effective method in reducing S, and therefore $\lambda_I \approx S\, \hbar\langle \omega_I \rangle$, (c.f. Eqs. 6 and 7) as shown in Table 1. Another feature that leads to a reduced S (see Fig. 3(a)) is the nonbonding character of the molecules. Calculations suggest that the primary intramolecular mode appears along the conjugated carbon chains forming the backbone, indicated by the bold line tracing the conjugation path. The presence of nonbonding orbitals in the cyano, chloro or oxy groups introduce lone pair electrons that do not participate in bonding, and that avoid electron-phonon coupling. At the same time, the cyano and chloro groups attract electrons and reduce the charge density along the backbones, effectively reducing electron-phonon coupling.

A small, S, and intermolecular coupling λ_O in NFAs, leads to a reduced Gibbs free energy change $-\Delta E_{CT}$ for achieving a maximum k_{CT} than for the more compact fullerenes. In particular, HJs using BT-IC achieve a maximum k_{CT} at only ΔE_{CT} = 0.22 eV, which is slightly lower than IT-IC, of ΔE_{CT} = 0.35 eV. Equation 4 is applied to fit both Fig. 5 and the temperature

dependent results above T_X in Fig. 6 to obtain λ_O = 0.21 ± 0.03 eV and S = 0.30 ± 0.10 for BT-ClC (BT-IC)/donor HJs, and λ_O = 0.35 ± 0.11 eV and S = 0.54 ± 0.12 for IT-IC/donor HJs. In contrast, fullerene/donor HJs show an unconstrained fit where $\lambda_I + \lambda_O \geq 0.6$ eV.

Charge transfer states are characterized by the strength of electron-phonon coupling and reorganization energy, λ_{CT}, during recombination, that can be determined via their Franck-Condon shifts (see Fig. 7). The Franck-Condon shift is twice the total reorganization energy, [46] i.e. $E_{FC} \approx 2\lambda_{CT}$, yielding λ_{CT} = 0.11 eV for IT-IC/PBDBT compared to λ_{CT} = 0.24 eV for $PC_{71}BM$/PBDBT. This results in a higher k_{nr} for the latter system, according to Fig. 2. Thus, $\eta_{EL} = \frac{k_r}{k_r + k_{nr}}$ is higher in the IT-IC/PBDBT HJ as shown in Fig. S1. Calculations of the non-radiative recombination loss using Eq. 10 and η_{EL} of IT-IC/PBDBT and $PC_{71}BM$/PBDBT HJs result in a 0.05 ± 0.01 eV smaller ΔE_{nr} in the IT-IC system, suggesting to the generally higher power conversion efficiencies observed for NFA vs. fullerene based OPVs.

The foregoing analysis suggests molecular design strategies that can further reduce energy loss. Currently, all a-d-a-type NFAs have symmetric electron-withdrawing end groups that possess a nearly zero dipole moment. However, asymmetric electron withdrawing end groups in a-d-a molecules can provide freedom to tune the dipole moment and further reduce E_B, S, and λ_O by changing the effective intramolecular electron-hole separation and molecular packing in bulk heterojunctions. Additionally, the relationship between molecular dimension, rigidity and energy loss points to the benefits of increasing the molecular volume. However, there is a limit to the extent to which the length of the molecular backbone can be increased without bending, and hence terminating the effective conjugation length. Extending the conjugation into two and three dimensions can further reduce E_B, S, and λ_O, as compared to one-

dimensional conjugation used up to now. This additional degree of freedom may also enhance intermolecular π–π interactions along all directions, leading to increased charge carrier mobilities. Indeed, early demonstrations of increasing the molecular volume in two dimensions based on dithienopicenocarbazole-based a-d-a-type [11] or spiro-fused perylene diimide NFAs [47] provide an illustration of the benefit of this strategy.

VI. Conclusions

This work presents a theory that connects molecular structure of a wide range of fullerenes and nonfullerene acceptors to energy losses in the charge photogeneration process at organic heterojunctions. Based on a combination of DFT, semi-classical Marcus theory and quantum mechanics, derived universal relationships connect the polarizabilities and exciton binding energies to molecular geometry. The large conjugated volumes along with the juxtaposition of electron donating and withdrawing groups characteristic of thiophene-based NFAs leads to significant decreases of their exciton binding energy, intra- and intermolecular electron-phonon couplings, compared to more compact and symmetric fullerenes. As a result, HJs employing NFAs, such as BT-IC(BT-ClC) and IT-IC, reach a maximum k_{CT} at a small CT state energy loss of only ΔE_{CT}=0.22 and 0.35 eV, respectively, compared to that for fullerenes with $\Delta E_{CT} \geq$ 0.6 eV. Furthermore, nonradiative recombination losses are concomitantly reduced in NFAs. Semi-classical Marcus theory is applied to quantify the impact of exciton binding energy and electron-phonon coupling on both ΔE_{CT} and ΔE_{nr}. A significant outcome of our analysis is to provide guidelines for the design of molecules with reduced energy losses by increasing the effective molecular volume. One particular approach is to extend the 1D molecular motifs currently employed in thiophene-based NFAs into two or three dimensions.

Ultimately, the use of these larger molecules should lead to higher OPV efficiencies when employed in HJs with appropriate donor, provided that their steric structure allows for the achievement of bulk heterojunction morphologies that encourage exciton dissociation and charge extraction.

Acknowledgement

This work was partially supported by the Office of Naval Research (X.L. experiments and analysis; K.D. analysis), and the Sun Shot Program of the Department of Energy (Y.L. material synthesis and analysis; S.R.F. analysis, project supervision).

Reference

[1] M. Knupfer, Exciton Binding Energies in Organic Semiconductors Appl. Phys. A Mater. Sci. Process. **77**, 623 (2003).

[2] H.-W. Li, Z. Guan, Y. Cheng, T. Lui, Q. Yang, C. S. Lee, S. Chen, and S. W. Tsang, On the Study of Exciton Binding Energy with Direct Charge Generation in Photovoltaic Polymers Adv. Electron. Mater. **2**, 1600200 (2016).

[3] S. Y. Leblebici, T. L. Chen, P. Olalde-Velasco, W. Yang, and B. Ma, Reducing Exciton Binding Energy by Increasing Thin Film Permittivity: An Effective Approach to Enhance Exciton Separation Efficiency in Organic Solar Cells ACS Appl. Mater. Interfaces **5**, 10105 (2013).

[4] S. Kraner, R. Scholz, C. Koerner, and K. Leo, Design Proposals for Organic Materials Exhibiting a Low Exciton Binding Energy J. Phys. Chem. C **119**, 22820 (2015).

[5] S. M. Menke, N. A. Ran, G. C. Bazan, and R. H. Friend, Understanding Energy Loss in Organic Solar Cells: Toward a New Efficiency Regime Joule **2**, 25 (2018).

[6] W. Zhao, D. Qian, S. Zhang, S. Li, O. Inganäs, F. Gao, and J. Hou, Fullerene-Free Polymer Solar Cells with over 11% Efficiency and Excellent Thermal Stability Adv. Mater. **28**, 4734 (2016).

[7] W. Chen and Q. Zhang, Recent Progress in Non-Fullerene Small Molecule Acceptors in Organic Solar Cells (OSCs) J. Mater. Chem. C **5**, 1275 (2017).

[8] Y. Li, L. Zhong, B. Gautam, H. J. Bin, J. D. Lin, F. P. Wu, Z. Zhang, Z. Q. Jiang, Z. G. Zhang, K. Gundogdu, Y. Li, and L. S. Liao, A Near-Infrared Non-Fullerene Electron Acceptor for High Performance Polymer Solar Cells Energy Environ. Sci. **10**, 1610 (2017).

[9] Y. Li, X. Liu, F. P. Wu, Y. Zhou, Z. Q. Jiang, B. Song, Y. Xia, Z. G. Zhang, F. Gao, O. Inganäs, Y. Li, and L. S. Liao, Non-Fullerene Acceptor with Low Energy Loss and High External Quantum Efficiency: Towards High Performance Polymer Solar Cells J. Mater. Chem. A **4**, 5890 (2016).

[10] C. B. Nielsen, S. Holliday, H.-Y. Chen, S. J. Cryer, and I. McCulloch, Non-Fullerene Electron Acceptors for Use in Organic Solar Cells Acc. Chem. Res. **48**, 2803 (2015).

[11] Z. Yao, X. Liao, K. Gao, F. Lin, X. Xu, X. Shi, and L. Zuo, Dithienopicenocarbazole-Based Acceptors for Efficient Organic Solar Cells with Optoelectronic Response Over 1000nm and an Extremely Low Energy Loss J. Am. Chem. Soc. **140**, 2054 (2018).

[12] D. Baran, T. Kirchartz, S. Wheeler, S. Dimitrov, M. Abdelsamie, J. Gorman, R. S. Ashraf, S. Holliday, A. Wadsworth, N. Gasparini, P. Kaienburg, H. Yan, A. Amassian, C. J. Brabec, J. R. Durrant, and I. McCulloch, Reduced Voltage Losses Yield 10% Efficient Fullerene Free Organic Solar Cells with >1 V Open Circuit Voltages Energy Environ. Sci. **9**, 3783 (2016).

[13] B. He, B. Yang, M. A. Kolaczkowski, C. A. Anderson, L. M. Klivansky, T. L. Chen, M. A. Brady, and Y. Liu, Molecular Engineering for Large Open-Circuit ACS Energy Lett. **3**, 1028 (2018).

[14] Y. Wang, D. Qian, Y. Cui, H. Zhang, J. Hou, K. Vandewal, T. Kirchartz, and F. Gao, Optical Gaps of Organic Solar Cells as a Reference for Comparing Voltage Losses Adv. Energy Mater. **8**, 1801352 (2018).

[15] J. Liu, S. Chen, D. Qian, B. Gautam, G. Yang, J. Zhao, J. Bergqvist, F. Zhang, W. Ma, H. Ade, O. Inganäs, K. Gundogdu, and H. Yan, Fast Charge Separation in a Non-Fullerene

Organic Solar Cell with a Small Driving Force Nat. Energy **1**, 16089 (2016).

[16] B. P. Rand, D. P. Burk, and S. R. Forrest, Offset Energies at Organic Semiconductor Heterojunctions and Their Influence on the Open-Circuit Voltage of Thin-Film Solar Cells Phys. Rev. B **75**, 115327 (2007).

[17] D. C. Coffey, B. W. Larson, A. W. Hains, J. B. Whitaker, N. Kopidakis, O. V. Boltalina, S. H. Strauss, and G. Rumbles, An Optimal Driving Force for Converting Excitons into Free Carriers in Excitonic Solar Cells J. Phys. Chem. C **116**, 8916 (2012).

[18] A. J. Ward, A. Ruseckas, M. M. Kareem, B. Ebenhoch, L. A. Serrano, M. Al-Eid, B. Fitzpatrick, V. M. Rotello, G. Cooke, and I. D. W. Samuel, The Impact of Driving Force on Electron Transfer Rates in Photovoltaic Donor-Acceptor Blends Adv. Mater. **27**, 2496 (2015).

[19] T. Linderl, T. Zechel, M. Brendel, D. Moseguí González, P. Müller-Buschbaum, J. Pflaum, and W. Brütting, Energy Losses in Small-Molecule Organic Photovoltaics Adv. Energy Mater. **7**, 1 (2017).

[20] J. Benduhn, K. Tvingstedt, F. Piersimoni, S. Ullbrich, Y. Fan, M. Tropiano, K. A. McGarry, O. Zeika, M. K. Riede, C. J. Douglas, S. Barlow, S. R. Marder, D. Neher, D. Spoltore, and K. Vandewal, Intrinsic Non-Radiative Voltage Losses in Fullerene-Based Organic Solar Cells Nat. Energy **2**, (2017).

[21] M. Azzouzi, J. Yan, T. Kirchartz, K. Liu, J. Wang, H. Wu, and J. Nelson, Non-Radiative Energy Losses in Bulk-Heterojunction Organic Photovoltaics Phys. Rev. X **8**, 31055 (2018).

[22] R. A. Marcus and N. Sutin, Electron Transfers in Chemistry and Biology Biochim.

Biophys. Acta **811**, 265 (1985).

[23] J. Bixon, M., Jortner, *Electron Transfer- From Isolated Molecules to Biomolecules* (Wiley: New York, 1999).

[24] H. Bässler and A. Köhler, "Hot or Cold": How Do Charge Transfer States at the Donor-Acceptor Interface of an Organic Solar Cell Dissociate? Phys. Chem. Chem. Phys. **17**, 28451 (2015).

[25] K. Vandewal, S. Albrecht, E. T. Hoke, K. R. Graham, J. Widmer, J. D. Douglas, M. Schubert, W. R. Mateker, J. T. Bloking, G. F. Burkhard, A. Sellinger, J. M. J. Fréchet, A. Amassian, M. K. Riede, M. D. Mcgehee, D. Neher, and A. Salleo, Efficient Charge Generation by Relaxed Charge-Transfer States at Organic Interfaces Nat. Mater. **13**, 63 (2013).

[26] R. A. Marcus, On Theory of Electron-Transfer Reactions. VI. Unified Treatment for Homogeneous and Electrode Reactions J. Chem. Phys. **43**, 679 (1965).

[27] U. Rau, Reciprocity Relation between Photovoltaic Quantum Efficiency and Electroluminescent Emission of Solar Cells Phys. Rev. B **76**, 085303 (2007).

[28] R. Englman and J. Jortner, The Energy Gap Law for Radiationless Transitions in Large Molecules Mol. Phys. **18**, 285 (1970).

[29] M. J. Frisch, G. W. Trucks, H. B. Schlegel, G. E. . Scuseria, M. A. Robb, G. Cheeseman, J. R. Scalmani, V. Barone, B. Mennucci, G. A. Petersson, H. Nakatsuji, M. Caricato, X. Li, H. P. Hratchian, A. F. Izmaylov, J. Bloino, G. Zheng, J. L. Sonnenberg, M. Hada, and M. Ehara, Gaussian 09, Revision E.01 **Gaussian09**, revision E.01; (2009).

[30] M. A. Alamoudi, J. I. Khan, Y. Firdaus, K. Wang, D. Andrienko, P. M. Beaujuge, and F.

Laquai, Impact of Nonfullerene Acceptor Core Structure on the Photophysics and Efficiency of Polymer Solar Cells ACS Energy Lett. **3**, 802 (2018).

[31] J. L. Borioni, M. Puiatti, D. M. A. Vera, and A. B. Pierini, In Search of the Best DFT Functional for Dealing with Organic Anionic Species Phys. Chem. Chem. Phys. **19**, 9189 (2017).

[32] S. A. Lopez, B. Sanchez-lengeling, J. D. G. Soares, and A. Aspuru-Guzik, Design Principles and Top Non-Fullerene Acceptor Candidates for Organic Photovoltaics Joule **1**, 857 (2017).

[33] A. Wadsworth, M. Moser, A. Marks, M. S. Little, N. Gasparini, C. J. Brabec, D. Baran, and I. McCulloch, Critical Review of the Molecular Design Progress in Non-Fullerene Electron Acceptors towards Commercially Viable Organic Solar Cells Chem. Soc. Rev. (2018).

[34] H. Gao, Y. Sun, X. Wan, X. Ke, H. Feng, B. Kan, Y. Wang, Y. Zhang, C. Li, and Y. Chen, A New Nonfullerene Acceptor with Near Infrared Absorption for High Performance Ternary-Blend Organic Solar Cells with Efficiency over 13 % Adv. Sci. **5**, 1800307 (2018).

[35] L. Zhu, Y. Yi, and Z. Wei, Exciton Binding Energies of Nonfullerene Small Molecule Acceptors□: Implication for Exciton Dissociation Driving Forces in Organic Solar Cells J. Phys. Chem. C **122**, 22309 (2018).

[36] Q. Wang, Y. Li, P. Song, R. Su, F. Ma, and Y. Yang, Non-Fullerene Acceptor-Based Solar Cells: From Structural Design to Interface Charge Separation and Charge Transport Polymers **9**, 692 (2017).

[37] J. Tomasi, B. Mennucci, and R. Cammi, Quantum Mechanical Continuum Solvation Models Chem. Rev. **105**, 2999 (2005).

[38] See Supplemental Material at for additional information of molecular structures, polarizability and CT state EL quantum yield.

[39] K. Vandewal, K. Tvingstedt, A. Gadisa, O. Inganäs, and J. V. Manca, Relating the Open-Circuit Voltage to Interface Molecular Properties of Donor:Acceptor Bulk Heterojunction Solar Cells Phys. Rev. B **81**, 125204 (2010).

[40] J. Y. Lee, B. J. Mhin, S. Mukamel, and K. S. Kim, Size Scaling of Intramolecular Charge Transfer Driven Optical Properties of Substituted Polyenes and Polyynes J. Chem. Phys. **119**, 7519 (2003).

[41] A. Slama-Schwok, M. Blanchard-Desce, and J.-M. Lehn, Intramolecular Charge Transfer in Donor-Acceptor Molecules J. Phys. Chem. **94**, 3894 (1990).

[42] J. Rissler, Effective Conjugation Length of π-Conjugated Systems Chem. Phys. Lett. **395**, 92 (2004).

[43] C. Van Dyck, T. J. Marks, and M. A. Ratner, Chain Length Dependence of the Dielectric Constant and Polarizability in Conjugated Organic Thin Films ACS Nano **11**, 5970 (2017).

[44] P. Chopra, L. Carlacci, H. F. King, and P. N. Prasad, Ab Initio Calculations of Polarizabilities and Second Hyperpolarizabilities of Organic Molecules with Extended Ir-Electron Conjugation J. Phys. Chem. **93**, 7120 (1989).

[45] Ş. Atahan-Evrenk and A. Aspuru-Guzik, *Prediction and Calculation of Crystal Structures: Methods and Applications* (2014).

[46] M. De Jong, L. Seijo, A. Meijerink, and F. T. Rabouw, Resolving the Ambiguity in the

Relation between Stokes Shift and Huang – Rhys Parameter Phys. Chem. Chem. Phys. **17**, 16959 (2015).

[47] G. Gao, N. Liang, H. Geng, W. Jiang, H. Fu, J. Feng, J. Hou, X. Feng, and Z. Wang, Spiro-Fused Perylene Diimide Arrays J. Am. Chem. Soc. **139**, 15914 (2017).

Table

Table. 1. The intramolecular reorganization energy due to electron transfer of archetypical fullerenes and NFAs.

	$PC_{71}BM$	IDT-IC	IDTIDT-IC	BT-ClC
λ_I^- (eV)	0.180	0.179	0.101	0.157

Figure captions

Figure 1. Energy diagrams of (a) charge transfer from the acceptor exciton (A^*) to the charge transfer (CT) state (A^-/D^+), and (b) non-radiative recombination from the CT state (A^-/D^+) to the ground state (A/D). The Gibbs free energies are ΔE_{CT} in (a) and E_{CT} in (b). Symmetric parabolic potentials are assumed for the initial and final states. The vibrational levels (n , n', and n''= {0, 1, 2 …}) are equally spaced. Equilibrium configurations of A^*/D, A^-/D^+, and A/D manifolds are indicated by Q_1, Q_2 and Q_3, respectively.

Figure 2. Charge transfer rate, k_{CT}, vs. the energy loss on CT state formation, ΔE_{CT} as functions of (a) the intermolecular reorganization energy, λ_0, and (b) intramolecular coupling strength, S. (c) Non-radiative recombination rate, k_{nr}, vs. E_{CT} as functions of λ_0 and (d) S.

Figure 3. (a) The molecular structure of BT-ClC. The red bold line traces the electron conjugation path comprising alternating C-C single and double bonds. Blue dashed circles indicate the electron-rich (i.e. oxy-) and deficient (i.e. chloro- and cyano-) moieties that affects the electron distributions in the molecules. (b) The electron and hole density distributions along the molecular length of BT-ClC calculated using density functional theory (DFT). (c) The molecular structural formulae of IDT-IC and IDTIDT-IC, that have different length of the electron-donating cores as indicated in the shaded regions.

Figure 4. (a) Exciton binding energy, E_B, found via DFT vs. effective molecular volume for several acceptor molecules indicated in legend, and whose molecular formulae are in Supplementary Information. [38] The red solid line is a fit assuming electron confinement within the effective molecular volume for each molecule. The calculation assumes a dielectric parameter, f=5. 4. The shaded area is the 95% confidence band. The blue dashed line assumes f

depends on molecular polarizability from (b). The confidence limits of the calculations are shown by dotted lines. (b) The calculated molecular polarizability along the molecular longitudinal axis, α_{xx}, vs. the effective molecular length *l*. The dashed line is the fit using an empirical power-law described in text.

Figure 5. Measured k_{CT} vs. ΔE_{CT} for HJs comprising (a) 1. BT-IC/PBDBT, 2. BT-IC/J61, 3. BT-IC/P3HT, 4. BT-ClC/PCDTBT, 5. BT-ClC/PBDBT, 6. BT-ClC/J61, (b) 1. IT-IC/PCDTBT, 2. IT-IC/PBDBT, 3. IT-IC/J61, 4. IT-IC/P3HT, and (c) 1. $PC_{71}BM$/F8T2, 2. $PC_{71}BM$/F8, 3. $PC_{71}BM$/F8BT, 4. ICBA/F8T2, 5. $PC_{61}BM$/F8T2, 6. $PC_{61}BM$/F8, 7. $PC_{61}BM$/F8BT, 8. C_{70}/CBP, 9. C_{70}/TCTA, 10. C_{70}/NPD, and 11. C_{70}/TPTPA. The dashed lines in (a) and (b) are the fits using semi-classical Marcus theory (Eq. 4 in text). The blue dashed line in (c) is a guide to the eye. All molecular structural formulae are found in Supplementary Information. [38]

Figure 6. Measured k_{CT} vs. temperature, T, for (a) BT-IC/PBDBT and (b) IT-IC/PBDBT HJs. The dashed lines are the fits assuming thermal activation.

Figure 7. Electroluminescence (*EL*) and external quantum efficiency (*EQE*) spectra of OPVs based on (a) neat IT-IC, PBDBT, and their blended heterojunction. (b) Neat $PC_{71}BM$, PBDBT, and their blended heterojunction. The CT state emission at low energy is extracted from the EL spectra by subtracting the spectra from the neat layers. The CT state absorption spectra is extracted by a Gaussian fit of the *EQE* spectra along the low energy shoulders. The arrows between the short lines indicate the Franck-Condon shift, E_{FC}, of CT spectra.

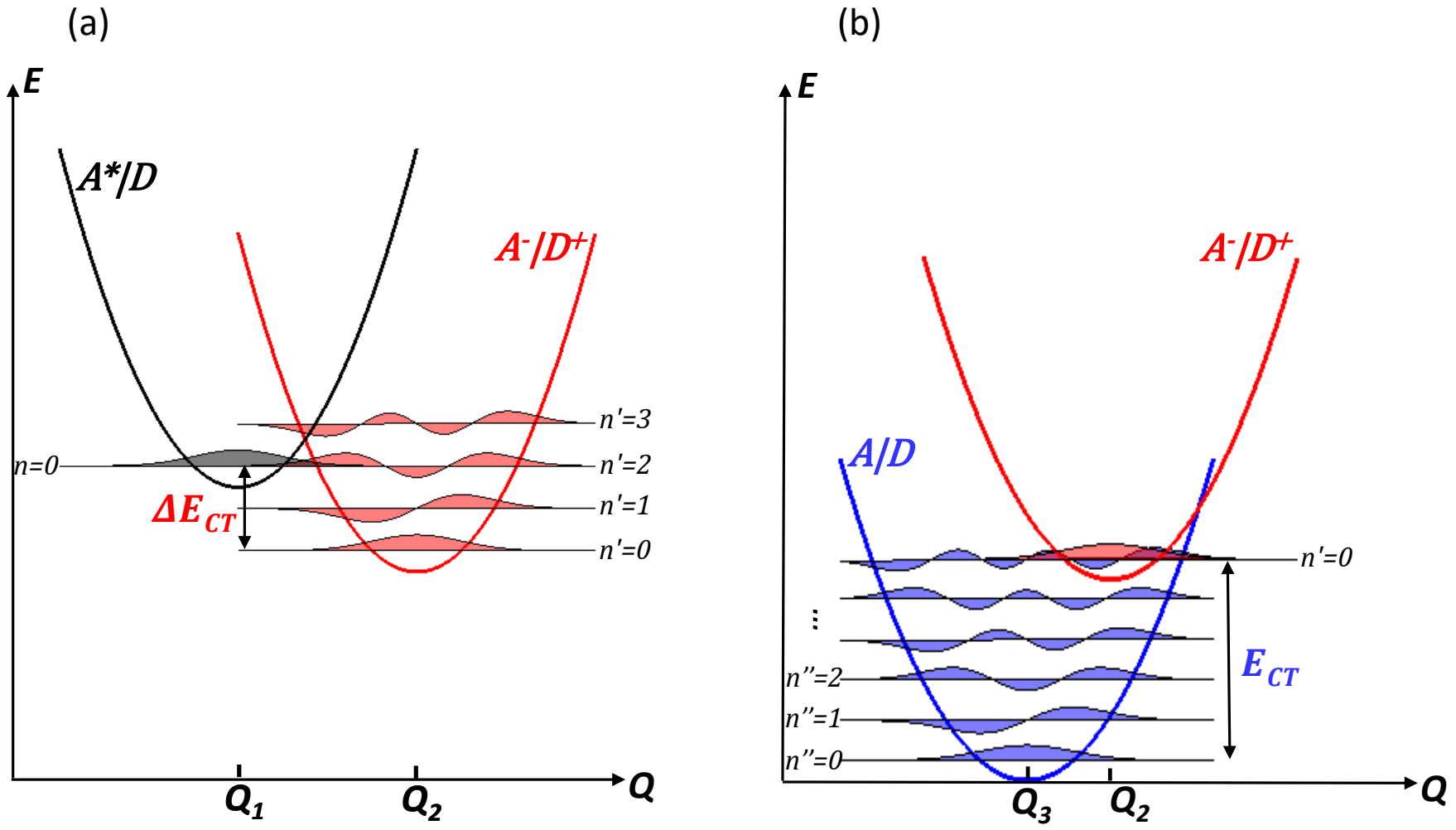
(a)
E
A*/D
A-/D+
n=0
n′=3
n′=2
n′=1
n′=0
ΔE CT
Q1
Q2
Q
(b)
E
A-/D+
A/D
n′=0
n″=2
n″=1
n″=0
E CT
Q3
Q2
Q

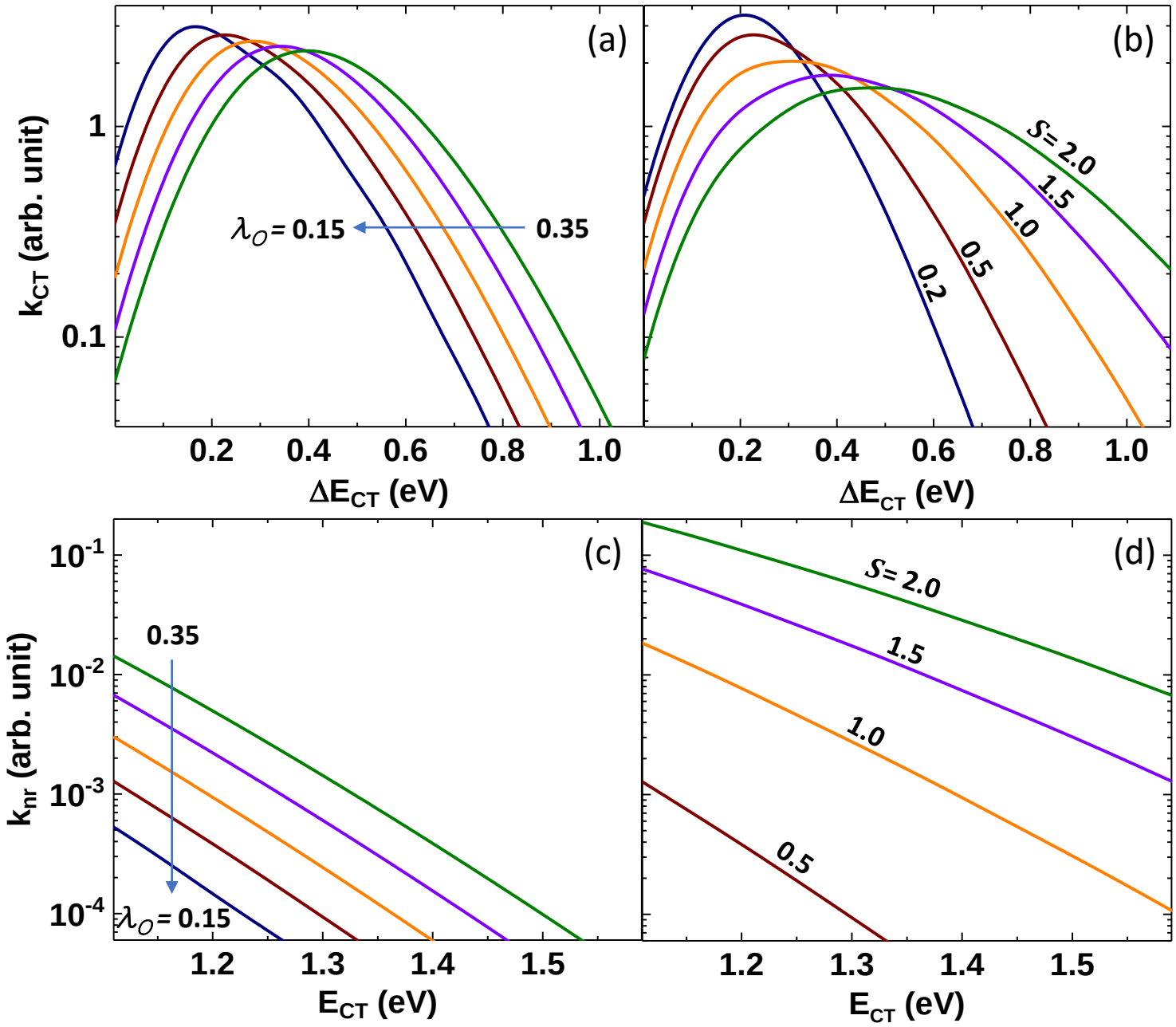
(a)
(b)
(c)
(d)
k_{CT} (arb. unit)
1
0.1
λ_O = 0.15
0.35
S= 2.0
1.5
1.0
0.5
0.2
0.2
0.4
0.6
0.8
1.0
ΔE_{CT} (eV)
k_{nr} (arb. unit)
10^{-1}
10^{-2}
10^{-3}
10^{-4}
1.2
1.3
1.4
1.5
E_{CT} (eV)

(a)

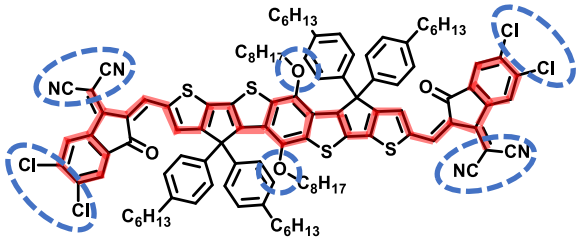

BT-ClC

(b)

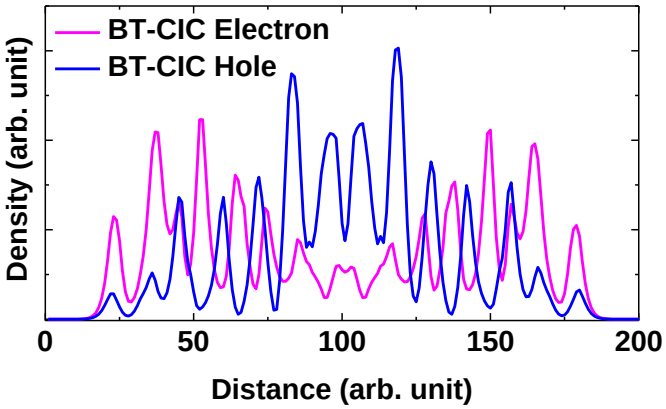

(c)

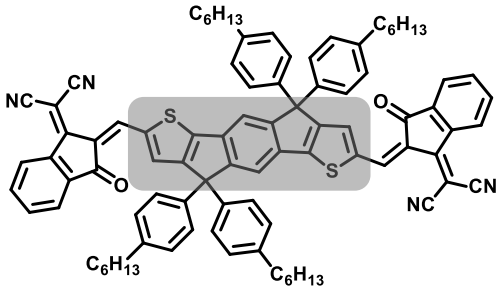

IDT-IC

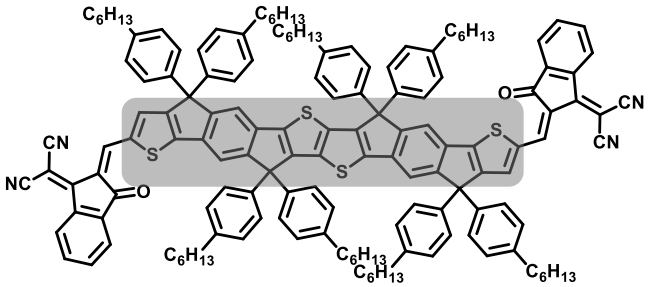

IDTIDT-IC

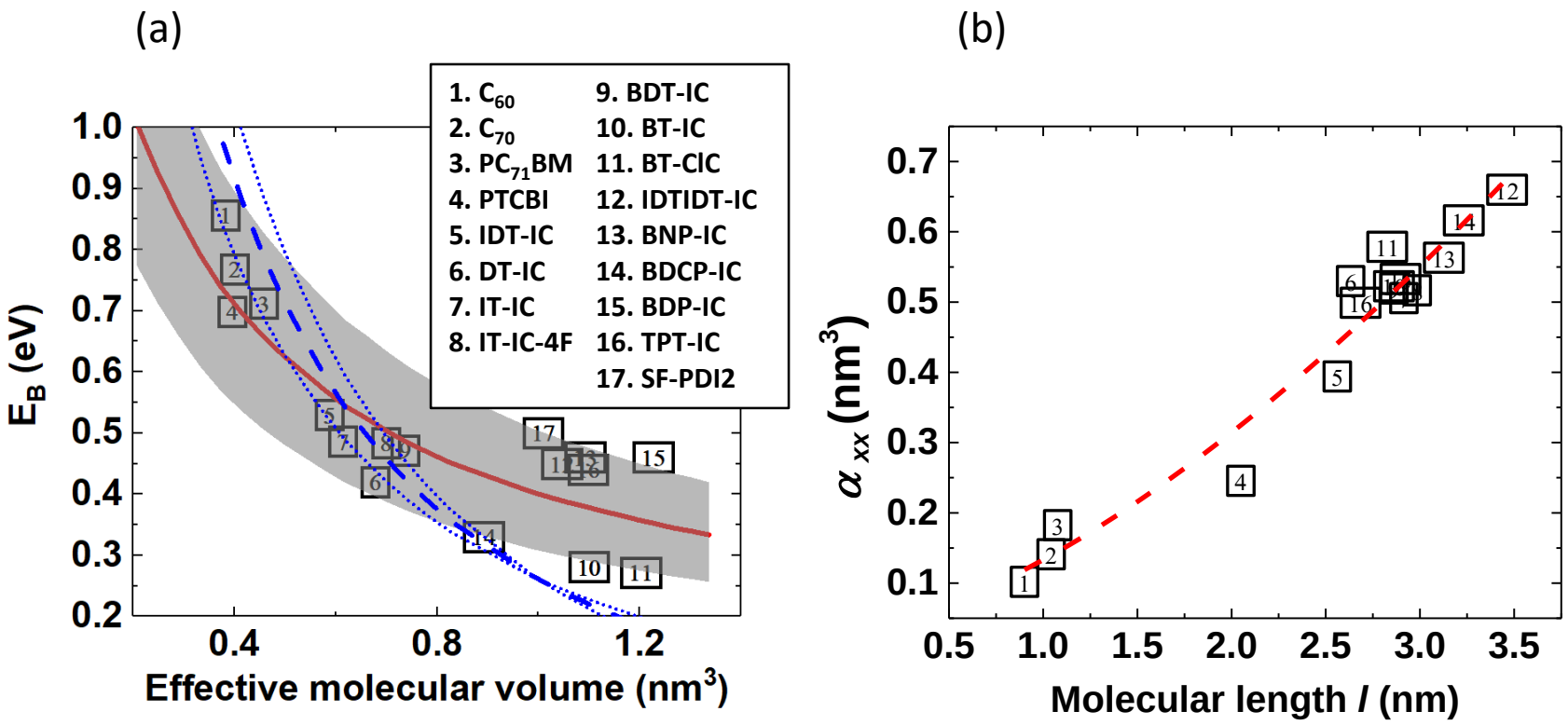
(a)
(b)
1. C60
2. C70
3. PC71BM
4. PTCBI
5. IDT-IC
6. DT-IC
7. IT-IC
8. IT-IC-4F
9. BDT-IC
10. BT-IC
11. BT-ClC
12. IDTIDT-IC
13. BNP-IC
14. BDCP-IC
15. BDP-IC
16. TPT-IC
17. SF-PDI2
E_B (eV)
Effective molecular volume (nm^3)
α_xx (nm^3)
Molecular length l (nm)

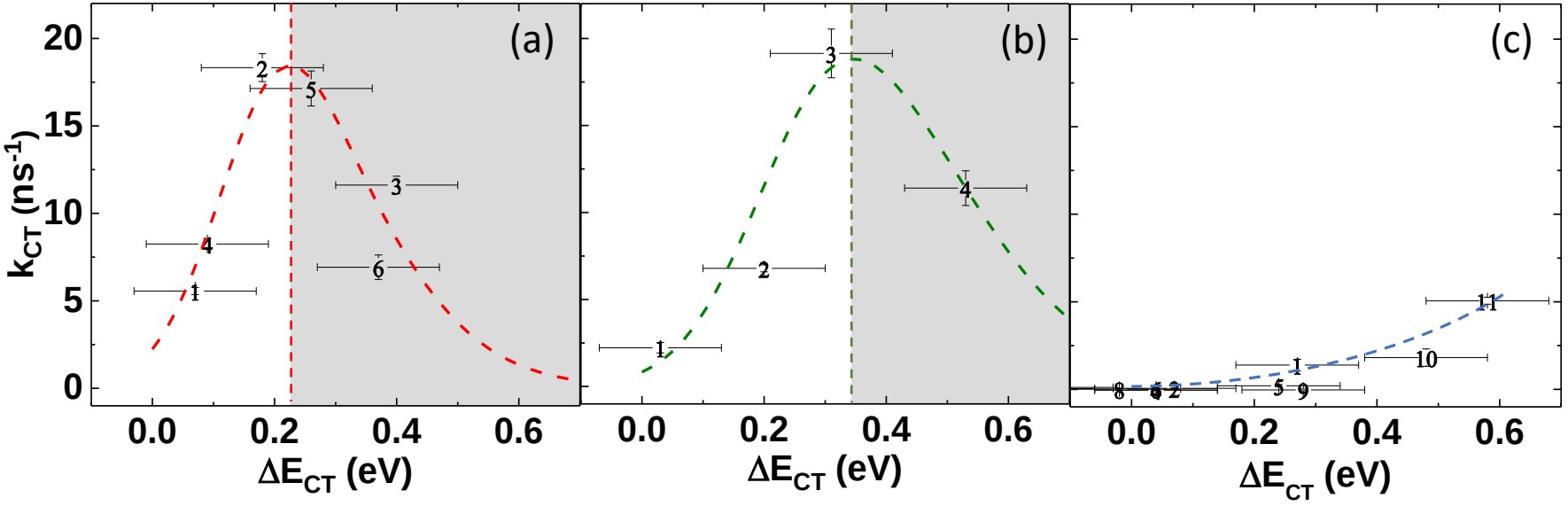
(a)
(b)
(c)
k_{CT} (ns^{-1})
ΔE_{CT} (eV)
ΔE_{CT} (eV)
ΔE_{CT} (eV)
0
5
10
15
20
0.0
0.2
0.4
0.6
1
2
3
4
5
6
1
2
3
4
1
2
5
8
9
10
11

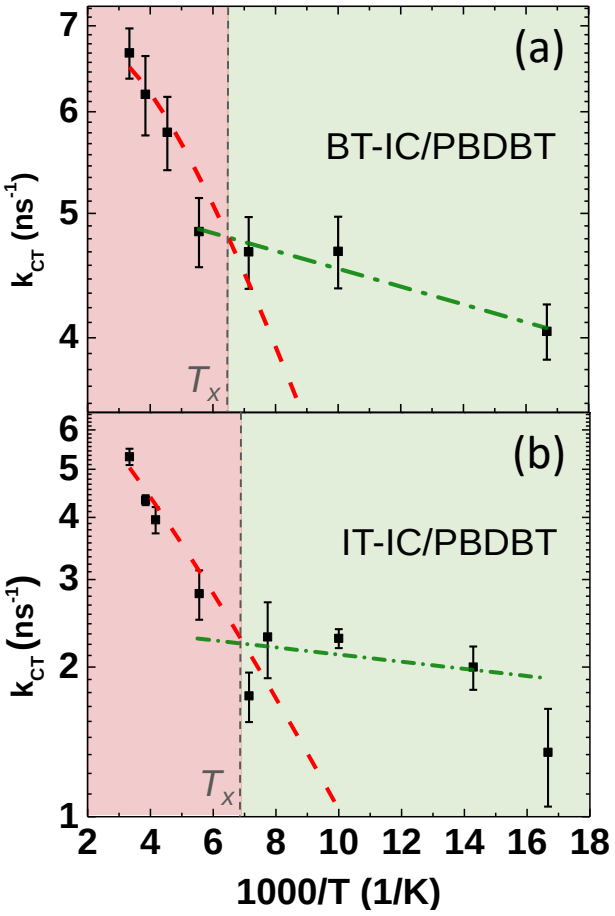
(a)
BT-IC/PBDBT
(b)
IT-IC/PBDBT
k_{CT} (ns^{-1})
T_x
1000/T (1/K)
2
4
6
8
10
12
14
16
18
1
2
3
4
5
6
7

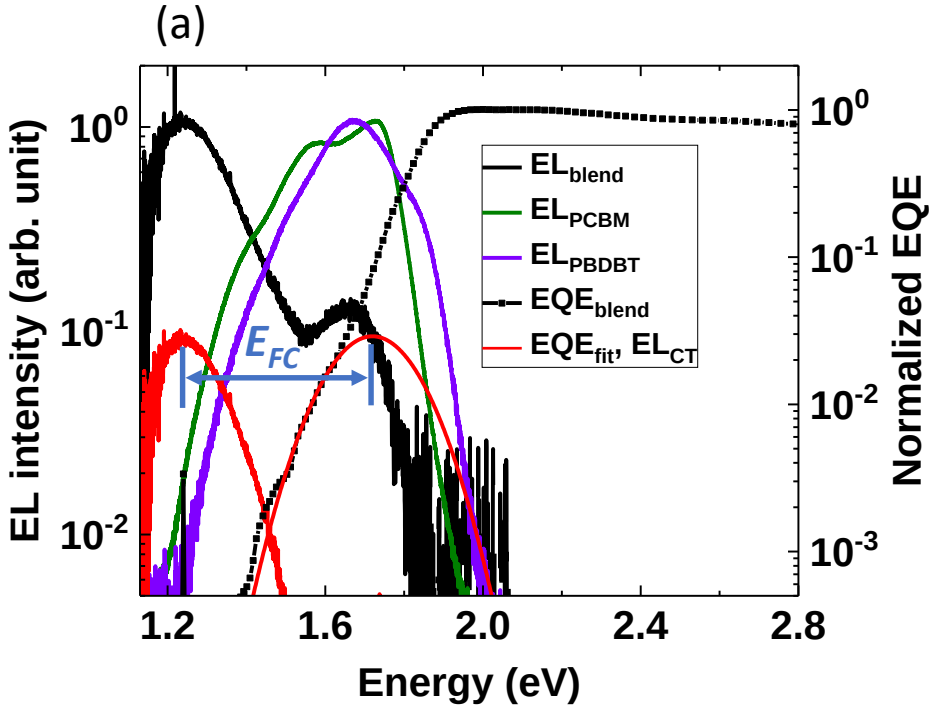
(a)
EL intensity (arb. unit)
Normalized EQE
Energy (eV)
EL_blend
EL_PCBM
EL_PBDBT
EQE_blend
EQE_fit, EL_CT
E_FC

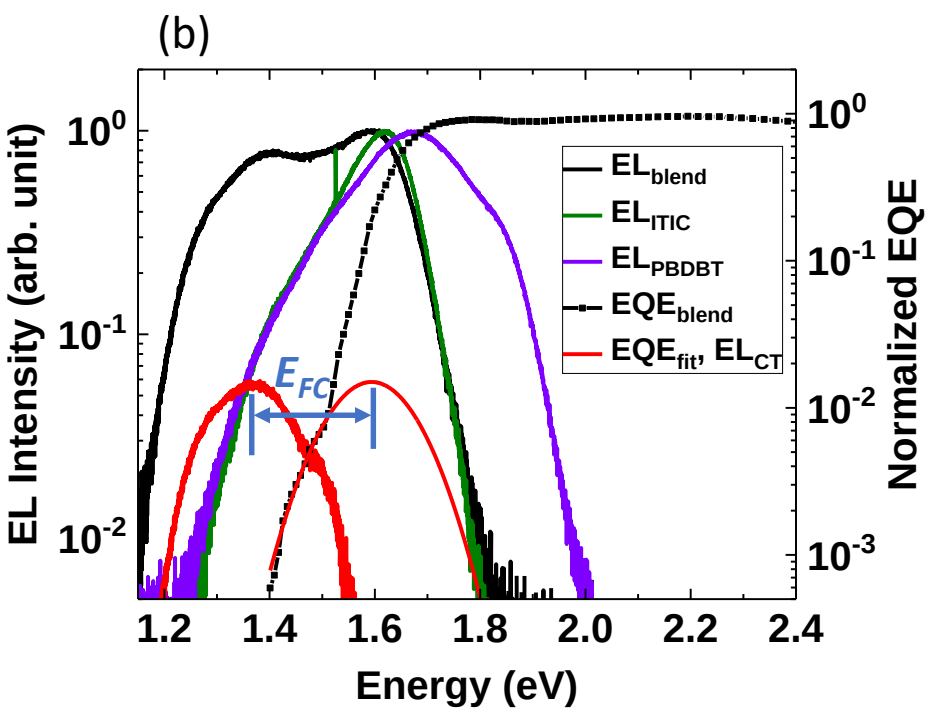
(b)
EL Intensity (arb. unit)
Normalized EQE
Energy (eV)
EL_blend
EL_ITIC
EL_PBDBT
EQE_blend
EQE_fit, EL_CT
E_FC